

## The Galactic Magnetic Field and UHECR Deflections

---

Michael Unger <sup>a,\*</sup> and Glennys R. Farrar <sup>b</sup>

<sup>a</sup>*Institute for Astroparticle Physics, Karlsruhe Institute of Technology, Karlsruhe 76344, Germany*

<sup>b</sup>*Center for Cosmology and Particle Physics, Department of Physics, New York University, NY 10003, USA*

*E-mail:* [michael.unger@kit.edu](mailto:michael.unger@kit.edu), [gf25@nyu.edu](mailto:gf25@nyu.edu)

Ultrahigh-energy cosmic rays (UHECRs) experience deflections as they traverse the Galactic magnetic field (GMF), which must be accounted for when tracing them back to their sources. After briefly summarizing our results on uncertainties in cosmic-ray deflections from the UF23 ensemble of GMF models (Unger & Farrar, 2024), we report a new preliminary fit of the GMF including foreground emission from the Local Bubble. This fit uses the analytic model of Pelgrims et al. (2024) for the magnetic field in the thick shell Galactic bubbles. We also discuss how variations in toroidal halo field modeling account for the key differences between the Jansson & Farrar (2012) GMF model and the UF23 ensemble.

We also extend our previous analysis of the origin of the highest-energy “Amaterasu” event observed by the Telescope Array to include the four highest-energy events detected by the Pierre Auger Observatory. Amaterasu and PAO070114 are the UHECR events with the smallest localization uncertainties of 4.7% and 2.4%, respectively. Neither of their back-tracked directions aligns with any compelling candidate for a continuous UHECR accelerator. This strengthens the evidence that at least a fraction of the highest energy events originate from transient sources.

*7th International Symposium on Ultra High Energy Cosmic Rays (UHECR2024)  
17-21 November 2024  
Malargüe, Mendoza, Argentina*

---

\*Speaker

## 1. The Coherent Magnetic Field of the Milky Way

A good understanding of the the coherent magnetic field of the Galaxy (GMF) is important to study the impact of magnetic deflections on the arrival directions of extragalactic ultrahigh-energy cosmic rays. Determining the large-scale structure of the magnetic field of our Galaxy is particularly challenging since one must infer it from from the vantage point of Earth located inside the field. As demonstrated by the 2012 Jansson Farrar (JF12) model [1], the global structure of the GMF can be derived by fitting suitable parametric descriptions of the structure of the disk, toroidal and poloidal field, to the two astrophysical data sets that provide the strongest constraints on the coherent magnetic fields: the *rotation measures* (RMs) of extragalactic polarized radio sources and the *polarized intensity* (PI) of the synchrotron emission of cosmic-ray electrons in the Galaxy. The interpretation of this data relies on *auxiliary models* of the three-dimensional density of thermal electrons  $n_e$  and cosmic-ray electrons  $n_{\text{cre}}$  in the Galaxy. In Ref. [2] (UF23 in the following) we studied the combination of different data sets, auxiliary models and parametric functions and obtained an ensemble of GMF models that reflect the uncertainties and degeneracies inherent in the inference of the global field structure from the limited information provided by RM and PI data. We have narrowed down these model variants to a few benchmark models that encompass the largest differences within the ensemble as summarized in Table 1.

In addition to the ensemble of eight models in UF23 we introduce here a ninth model called `locBub`, in which we include the foreground synchrotron emission from the Local Bubble into the GMF fit, and a model called `asymT` discussed below. The local bubble is a cavity with a low density of gas within which the Sun is situated and which is thought to originate from multiple supernova explosions that occurred in the past 10-15 Myr. A first fit of the GMF including the Local Bubble was recently reported in Ref. [3] using an approximate functional form for a magnetic field compressed into a spherical shell. Here, we present a preliminary fit of the Local Bubble with the divergence-free analytic ‘‘SCO’’ model of Ref. [4].

As shown in Table 1, this new preliminary `locBub` fit results in a slightly better fit quality than any of the other model variants. The latitude of the direction of the fitted pre-explosion field

( $B_0 = 1.7 \mu\text{G}$ ) agrees well with the value obtained in Ref. [5] from dust polarization maps, but the longitude differs by  $\sim 40^\circ$ . The model parameters of this fit are close to the parameters of the base model, except for a 25% smaller ‘‘striation’’ factor (related to the contribution of anisotropic random fields to PI) and a different shape parameter of the poloidal X-field ( $p = 1.0$  instead of 1.4).

Furthermore, we investigated in detail the differences in the toroidal halo field of JF12 and the UF23 models, to identify the main reason for the discrepancies in the magnification maps reported in Ref. [6]. Apart from the `twistX` variant, all the models use the same functional form for the toroidal field. However, the JF12 model, which lacked the flexible spiral arm geometry of the UF23

**Table 1:** Overview of model variations discussed in this paper. The first eight rows are the UF23 model variations, and the last two rows refer to models discussed in these proceedings.

name	variation	$\chi^2/\text{ndf}$
base	fiducial model	1.22
expX	radial dependence of X-field	1.30
spur	replace grand spiral by local spur (Orion arm)	1.23
neCL	change $n_e$ from YMW16 to NE2001	1.19
twistX	unified halo model via twisted X-field	1.26
nebCor	$n_e$ - $B$ correlation	1.22
cre10	$n_{\text{cre}}$ vertical scale height	1.22
synCG	use COSMOGLOBE synchrotron maps	1.50
asymT	as neCL, but forced N-S-asymmetric toroidal halo	1.22
locBub	local bubble (preliminary, spherical approximation)	1.17

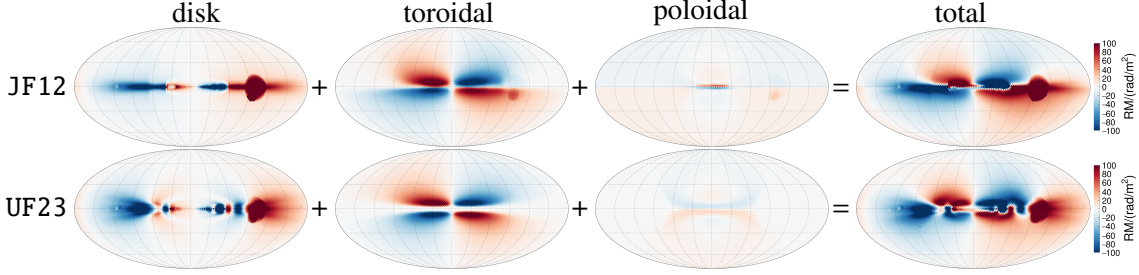


**Figure 1:** Sky maps of predicted Rotation Measures of JF12 (top row) and UF23 neCL (bottom row). The first three columns show the contributions of the disk, toroidal and poloidal model components and the right-most column shows their sum.

models, required a significantly larger radial extent in the Galactic South than in the North. Both models have azimuthal fields of opposite direction in the Northern and Southern hemispheres, as needed to describe the observed anti-symmetric pattern in longitude  $\ell$  and latitude  $b$  of rotation measures. However, the radial extent of the toroidal field in the two hemispheres was found to be the same in the UF23 model fit ( $r_t = 10.1$  kpc, with a transition width of 1.1 kpc in neCL). In the case of the JF12 model, the radial extent differs in the Galactic North and South ( $r_{tN} = 9.2$  kpc  $r_{tS} = 17.5$  kpc with a sharp transition width of 0.14 kpc); the different radial extents of the toroidal halos directly leads to the “butterfly pattern” of the observed rotation measures,  $RM(\ell, b) \approx \begin{pmatrix} + & - & + \\ - & - & + \end{pmatrix}$ , i.e. to the smaller extent in longitude of the central anti-symmetric RM features in the North than in the South. In UF23, on the other hand, this pattern is achieved by the superposition of a halo with a symmetric geometry and the field of the local spiral arm, similar to [8]. This important difference is best appreciated by comparing how the individual model components add up to the full RM, as shown in Fig. 1 (see e.g. Fig. 2(a) in [2] for the RM pattern in data).

Since the JF12 model does not describe the contemporary RM and synchrotron data well ( $\Delta\chi^2 \approx +1000$  with respect to UF23), it is difficult to assess whether its lack of N-S symmetry in the radial extent of the toroidal fields is a viable alternative to the one of the UF23 models. We therefore refitted the UF23 model forcing the fit to converge to the local minimum of an asymmetric halo geometry, made possible by fixing the toroidal width to 0.14 kpc. The resulting forced model variant has  $\Delta\chi^2 = +171$  with respect to neCL and  $\Delta\chi^2 = +244$  with respect to base when using the YWM16 thermal electron model. While a N-S symmetric toroidal halo component is appealing, being a natural result of the radial and vertical shear of the poloidal field as in the twistX variant, the  $\chi^2$  difference between the models is in the ballpark of the differences of UF23 model variants, see Table 2 in [2]. Therefore, we cannot exclude the possibility of an asymmetric halo with high confidence based on the extragalactic RMs alone. Note that the analysis of pulsar RMs in Ref. [7] favors a North-South symmetric halo, but relies to a large extent on the validity of pulsar distance estimates based on their dispersion measures and assumed structure of the thermal electron distribution.

For future reference, if a model with a JF12-type asymmetric halo is required that fits the contemporary RM and synchrotron data, we list here the parameters of the asymT model tuned with the NE2001 thermal electron model,  $(\alpha, z_d, w_d, B_1, B_2, B_3, \phi_1, \phi_2, \phi_3, B_N, B_S, z_t, r_{tN}, r_{tS}, w_t, B_p, p, z_p, r_p, w_p, \xi) = (12.1, 0.6, 0.01, 1.57, 1.5, 3.5, 180, 156, 69, 2.28, -2.08, 3.6, 9.0, 15(> 11), 0.14, 0.94, 1.77, 3.34, 7.45, 0.17, 0.41)$ , with the usual units kpc,  $\mu\text{G}$  and degree, see [2] for a detailed description of these parameters.

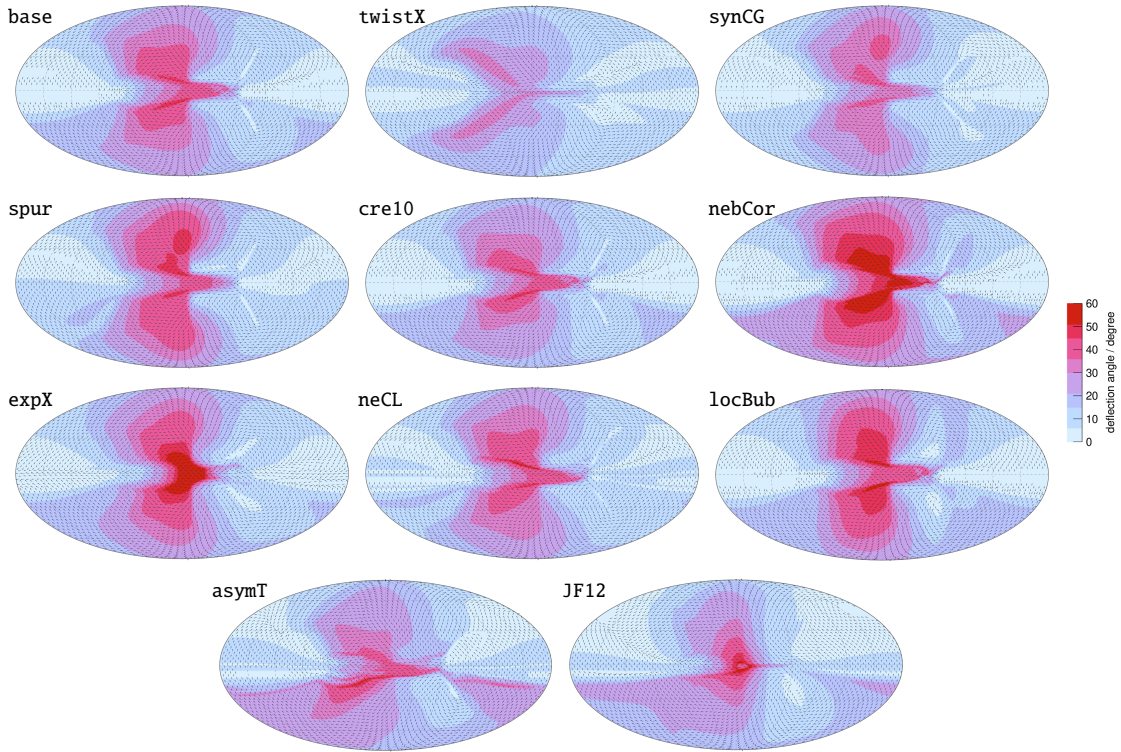


**Figure 2:** Angular deflections of ultrahigh-energy cosmic rays in the eight UF23 model variations, the preliminary fit with a local bubble presented at this conference, `asymT` model and JF12. Colors and arrows denote the size and direction of the deflection in the GMF following the particles from Earth to the edge of the Galaxy. Positions on the skymap denote arrival directions at Earth. The rigidity is  $2 \times 10^{19}$  V.

## 2. UHECR Deflections

Each of the UF23 model variations introduced in the previous section is a viable description of the GMF given the current RM and PI data, and the differences between the models gives an estimate of the lower limit on the uncertainty of our knowledge of the magnetic field of the Galaxy.

In Fig. 2 we show sky maps of the *deflection angle* at a particle rigidity of 20 EV ( $1 \text{ EV} = 10^{18} \text{ V}$ ) for each of the eight UF23 models, `asymT`, the preliminary fit with a local bubble, and the JF12 model. These were obtained by backtracking to a galactocentric radius of  $r_{\text{max}} = 30 \text{ kpc}$ . The magnitude of the deflection angle is indicated by colors at each arrival direction at Earth on a HEALPIX grid with  $N_{\text{side}} = 64$ . The direction of the deflection is indicated by an arrow for a subset of directions on a  $N_{\text{side}} = 16$  grid if  $\theta_{\text{def}} > 1^\circ$ . As can be seen, at a rigidity of  $\mathcal{R} = 20 \text{ EV}$  all models, including the `asymT` and the preliminary `locBub` fit, exhibit qualitatively similar deflection patterns but with quantitative differences for each model. All models exhibit a left-right asymmetry with deflections being larger if the particle is back-tracked towards positive longitudes and smaller for negative longitudes. This is the consequence of the twisted nature of the halo field.

For a closer look at the differences between the models, we compare the back-tracked directions in Fig. 3 for a sampling of arrival directions. The particle rigidity is again 20 EV and the lines interpolate back-tracked directions at higher rigidities. This figure illustrates the similarity of the models, since in many directions all of them roughly agree on the overall direction of the deflection,

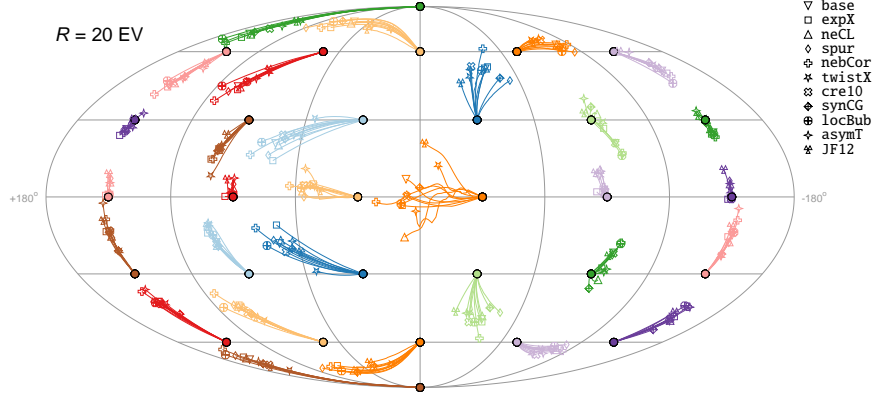


**Figure 3:** Angular deflections of ultrahigh-energy cosmic rays in the eight UF23 model variations, JF12 and the preliminary fit with a local bubble presented at this conference. The cosmic-ray rigidity is  $2 \times 10^{19}$  V. Filled circles denote a grid of arrival directions and the open symbols are the back-tracked directions at the edge of the Galaxy.

but also shows the model uncertainties, visible as a scatter in predicted directions for the ensemble of models. It is worth noting that the deflections predicted by the widely-used JF12 model are generally within the range of deflections predicted for the UF23 GMF models. This is not the case for the deflections calculated with the GMF model of [8] (not shown), due to the absence of a poloidal component in that model. The model components of the more recent KST24 model include a toroidal field with unequal North/South radial limits, very similar to the one of JF12 and asymT. The large magnetic field strength of the disk field of the KST24 model in the outer Galaxy is driven by the polarized intensity from the “Fan Region” – a feature in the synchrotron sky that is usually masked in fits of the global structure of the GMF. The magnetic field strength in this region is fully degenerate with the assumed local cosmic-ray electron density. Furthermore, even though the Fan Region is a large-scale feature in the outer Galaxy [9], it seems implausible that it is representative for the whole Perseus spiral arm, as assumed in the KST24 model. Therefore, we do not include this model in our evaluation of deflection uncertainties.

### 3. Localization of UHECR Events

Recently, we studied the localization of the “Amaterasu Particle”, the highest-energy event detected by the TA collaboration [10], using the UF23 model variations of the coherent Galactic magnetic field to backtrack its arrival direction at the edge of the Galaxy [11]. For this conference we apply the same analysis to the four highest-energy events from the Auger phase I data set [12]. These are listed in Table 2. The highest-energy event detected by the Pierre Auger Observatory so far has an energy of 166 EeV. For comparison, the nominal energy of the Amaterasu event is  $E = 244 \pm 29(\text{stat.})_{-76}^{+51}(\text{syst.})$  EeV using the TA energy scale. This value can be converted to the Auger energy scale using the energy-dependent TA-Augur relative cross-calibration factor estimated by the UHE spectrum working group in the common declination band,  $\Delta E_{\text{TA}}/E_{\text{TA}} = -0.09 - 0.2(\lg(E_{\text{TA}}/\text{eV}) - 19)$  [13]. The correction amounts to  $-36.7\%$  and the energy of the Amaterasu particle at the Auger energy scale is  $154 \pm 18(\text{stat.})$  EeV, compatible at  $1.2\sigma_{\text{syst}}$  with the nominal Amaterasu energy within the negative systematic uncertainty of  $\sigma_{\text{syst}} = -76$  EeV. Note

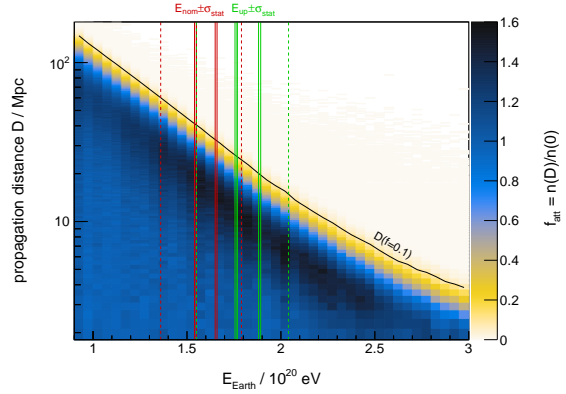
**Table 2:** The five highest-energy cosmic-ray particles detected with contemporary observatories. The quoted energies are at the Auger energy scale and the errors are statistical. See text for the localization uncertainty listed in the last two columns.

id	$E$ (EeV)	$\sigma_{\text{stat}}$ (EeV)	R.A. (degree)	Dec. (degree)	$\ell$ (degree)	$b$ (degree)	$\Omega_{\text{loc}} / 4\pi$ –	$\theta_{\text{loc}}$ (degree)
PAO191110	166	13	128.9	–52.0	269.1	–6.8	7.1%	31
PAO070114	165	13	192.9	–21.2	303.0	41.7	2.4%	18
PAO141021	155	12	102.9	–37.8	247.6	–16.2	6.3%	29
PAO200611	155	12	107.2	–47.6	258.3	–16.9	6.6%	29
TA210527	154	18	255.9	16.1	36.2	30.9	4.7%	25

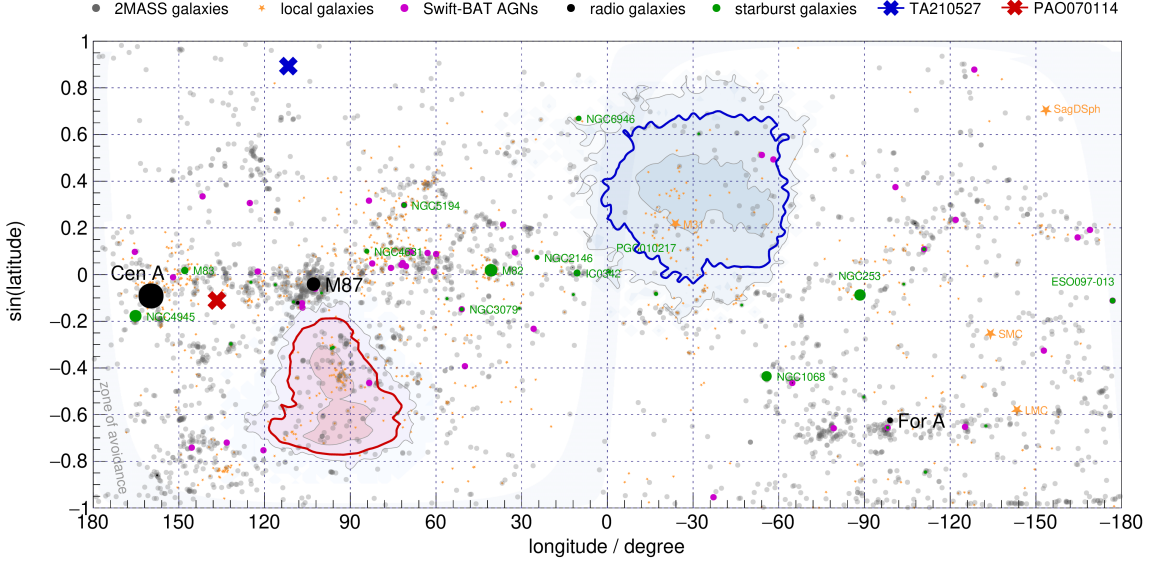
that this cross-calibration was obtained by the assumption that the cosmic-ray energy spectra in the Northern and Southern hemisphere are identical, which might not hold at UHE (see Refs. [14, 15] for further discussion).

Figure 4 shows a histogram of the propagation distance as a function of the UHECR energy at Earth, for  $\mathcal{R}_{\text{max}} = 10^{18.6}$  V. These were obtained with CRPROPA3 [16] assuming iron nuclei, see [11] for further details. The vertical solid lines mark the central energy values of the four events for the nominal and upper (+14%) Auger energy scale (note that two events at 155 EeV overlap, hence only four lines are visible). The one-standard-deviation of the statistical reconstruction uncertainty of the lowest- and highest-energy events is shown with dashed lines. We define the approximate edge of the source volume as the distance,  $D_{0.1}$ , at which the flux is attenuated by a factor of 10 relative to the case with no photo-interaction energy losses. At the average energy of the events of 160 EeV, the maximum source distance defined in this way is around 35 Mpc. At the one-sigma upper Auger energy scale, it is 23 Mpc. An even larger range of allowed distances is within one standard deviation of the statistical uncertainty of the energy reconstructions. In the following, we will concentrate on the results obtained at the nominal energy scale. We checked that the results at a  $\pm 1 \sigma_{\text{sys}}$  lead to similar conclusions.

We backtracked the arrival directions of the five highest energy cosmic-ray events through the Galactic magnetic field to identify the domain of highest source likelihood marginalizing over statistical rigidity uncertainty, coherent magnetic field models and different realizations of the random magnetic field of the Galaxy. The latter are generated with a root-mean-square field strength as given by the Planck-tune of the JF12 random field [17, 18] and we adopt an outer scale of the Kolmogorov turbulence of 100 pc, or equivalently a coherence length of 20 pc. We assumed that all particles were iron nuclei from the UHE end of the Peters cycle, see [11] for further discussion. In total, we backtracked 50 particles through 180 random field realizations per coherent field model, i.e. 9k particles per model and thus 72k particles per event. We then define as the *localization*



**Figure 4:** Propagation distances of CRs arriving at Earth, in each bin of energy as given on the  $x$ -axis of the plot, for iron injected with an  $\mathcal{R}_{\text{max}} = 10^{18.6}$  V energy spectrum (see text for details)



**Figure 5:** Contour lines of event localization of TA210527 (blue) and PAO070114 (red) in supergalactic coordinates. The gray lines are at contour levels of 0.01 and 0.5 and in thick blue/red line at 0.05. Points denote galaxies in the local volume ( $D < 11$  Mpc, orange) and galaxies within 35 Mpc from the 2MASS survey (gray), AGN (violet), radio galaxies (black) and starburst galaxies (green). The detected arrival direction of the particle is shown as a cross; the zone around the Galactic plane not covered in the 2MASS galaxy survey due to dust obscuration (“zone of avoidance”) is indicated with a very light gray area.

contour of the particle the backtracked directions at which the probability density drops below a factor 0.05 of the peak value of any model (see Eq. (2) in [11]). This contour encloses about 95% of all simulated particles (which is a numerical coincidence since in general contour levels do not correspond to confidence intervals).

The angular size of the corresponding event localization is listed in the two last columns of Table 2. Here  $\Omega_{loc}$  refers to the solid angle covered by the contour and the corresponding angular localization radius,  $\theta_{loc} \equiv \arccos(1 - \Omega_{loc}/2\pi)$ , contains the same area if the localization contour were circular. Note that these values are at the nominal Auger energy scale. The numerical value of the localization of TA210527 is somewhat larger in [11] (6.6% instead of 4.7%) since it includes the uncertainty in the TA energy scale.

The two events with the smallest localization uncertainty, TA210527 and PAO070114, are shown in Fig. 5 in supergalactic coordinates [19]. Due to their arrival directions far from the Galactic plane, their paths avoid regions of high magnetic field strength. However, the trajectories of PAO191110, PAO141021 and PAO200611 pass near the Galactic plane where the realization-to-realization variance of the random GMF is large. We stress that the deflections depend significantly on the random field, therefore the angular size of the localization regions can be expected to change to some degree when a future improved version of the coherent plus random GMF is developed, in which the random field for each of the suite of eight coherent GMF models is self-consistently fit to the synchrotron total intensity. The localization regions shown in Fig. 5 include variations across the eight coherent fields of UF23 but have not been extended to include the two new models *asymT* and *locBub*, introduced in these proceedings. However, the central deflection for these models falls well within the contours shown, except that the preliminary *locBub* model predicts a central

direction for PAO070114 that is slightly outside the contour at its lower left edge. However, this deviation does not qualitatively affect the subsequent discussion.

Fig. 5 also shows the position of galaxies within 35 Mpc, from the catalogs a) the flux-limited Two Micron All-Sky galaxy survey [20] cross-matched with the HyperLEDA distance database [21] (“2MASS” herein), b) the flux-limited *Swift*-BAT 105-month catalog of active galactic nuclei (AGN) observed in hard X-rays [22] and c) a sample of nearby starburst galaxies [23]. We also investigate d) radio galaxies from the volume-limited catalog [24]. Not all radio galaxies pass the UHE luminosity criterion [25–27] to be viable candidates for accelerators up to the rigidity of the Amaterasu particle and we therefore use only the subset identified as satisfying that requirement by [28]. For completeness, we also show galaxies from the “local volume catalog” [29], a volume-limited sample of galaxies within 11 Mpc.

PAO070114 is backtracked close to M87 but an origin in M87 has a low probability given that its location is outside of the tail of the contour, i.e. none of the 9000 backtracked particles per GMF model arrived at its position. Within the assigned uncertainty, none of the usual suspects of astrophysical candidate accelerators therefore can be associated with this event. This conclusion is similar to the one drawn in our previous analysis for TA’s Amaterasu particle, suggesting that both these UHECRs may originate in transient events in otherwise undistinguished galaxies. In addition, this analysis focuses attention on the possibility that Swift-BAT AGNs, perhaps via transients they host [27], may be the principle sources of UHECRs. All four of the highest energy Auger events contain at least one Swift-BAT AGN in their localization volume – albeit only on the edge of the localization region in the cases of PAO191110 and PAO070114. Moreover, using the central Auger energy assignment for Amaterasu brings a similarly peripheral AGN into its localization region. This does not mean that there is a Swift-BAT AGN source candidate for every one of the highest energy events – for that to be established, a single GMF and realization of the random field would have to be found with this feature for all, through a realization-by-realization query and a more detailed analysis of the energy-assignment-sensitivity of these conclusions.

## References

- [1] R. Jansson and G. R. Farrar *ApJ* **757** (2012) 14.
- [2] M. Unger and G. R. Farrar *ApJ* **970** (2024) 95.
- [3] A. Korochkin, D. Semikoz, and P. Tinyakov *A&A* **693** (2025) A284.
- [4] V. Pelgrims, M. Unger, and I. C. Mariş [arXiv:2411.06277](https://arxiv.org/abs/2411.06277), accepted in *A&A*.
- [5] V. Pelgrims *et al.* *A&A* **636** (2020) A17.
- [6] T. Bister, G. R. Farrar, and M. Unger *ApJL* **975** no. 1, (2024) L21.
- [7] J. Xu and J. L. Han *ApJ* **966** no. 2, (2024) 240.
- [8] M. S. Pshirkov *et al.* *ApJ* **738** (2011) 192.
- [9] A. S. Hill *et al.* *MNRAS* **467** no. 4, (2017) 4631.
- [10] R. Abbasi *et al.*, [Telescope Array Coll.] *Science* **382** no. 6673, (2024) 903.
- [11] M. Unger and G. R. Farrar *ApJ Lett.* **962** (2024) L5.
- [12] A. Abdul Halim *et al.*, [Pierre Auger Coll.] *ApJ Suppl.* **264** no. 2, (2023) 50.
- [13] D. Bergman *et al.*, [Pierre Auger, Telescope Array Coll.] *EPJ Web Conf.* **283** (2023) 2003.
- [14] A. Abdul Halim *et al.*, [Pierre Auger Coll.] [arXiv:2407.06874](https://arxiv.org/abs/2407.06874).
- [15] R. U. Abbasi *et al.*, [Telescope Array Coll.] [arXiv:2406.08612](https://arxiv.org/abs/2406.08612).
- [16] R. Alves Batista *et al.* *JCAP* **05** (2016) 038.
- [17] R. Jansson and G. R. Farrar *ApJ Lett.* **761** (2012) L11.
- [18] R. Adam *et al.*, [Planck Coll.] *A&A* **596** (2016) A103.
- [19] O. Lahav *et al.* *MNRAS* **312** no. 1, (2000) 166–176.
- [20] J. P. Huchra *et al.* *ApJ Suppl.* **199** (2012) 26.
- [21] D. Makarov *et al.* *A&A* **570** (2014) A13.
- [22] K. Oh *et al.* *ApJS* **235** no. 1, (2018) 4.
- [23] C. Lunardini *et al.* *JCAP* **2019** (2019) 073.
- [24] S. van Velzen *et al.* *A&A* **544** (2012) A18.
- [25] E. Waxman *Phys. Rev. Lett.* **75** (1995) 386.
- [26] R. D. Blandford *Phys. Scripta T* **85** (2000) 191.
- [27] G. R. Farrar and A. Gruzinov *ApJ* **693** (2009) 329.
- [28] J. H. Matthews *et al.* *MNRAS* **479** no. 1, (2018) L76.
- [29] I. D. Karachentsev, E. I. Kaisina, and D. I. Makarov *MNRAS* **479** (2018) 4136.